Inverse computational morphology of debris and alluvial fans

Yuan-Hung Damiel Chiu*[1], Tzu-Yin Kasha Chen†[1], and Hervé Capart‡[1]

[1]Dept of Civil Engineering and Hydrotech Research Institute, National Taiwan University, No. 1, Sec. 4, Roosevelt Rd., Taipei, 10617, Taiwan.

Abstract

In mountain areas, debris flows and fluvial transport often build up conical deposits at the confluence between steep tributaries and trunk rivers. The resulting debris and alluvial fans typically exhibit a well-defined relationship between slope or elevation and the distance from the fan apex. This relationship, however, becomes more difficult to characterize when fans are constrained by the topography of the valley, causing the paths of steepest slope to bend around obstacles. In previous work, a forward modeling approach was developed to reconstruct these more complex fan surfaces from an assumed elevation-distance profile. In this paper, we complement this forward algorithm with its inverse: a systematic, fast method to deduce the elevation-distance profile from either the observed fan topography or just its perimeter curve. Using the visibility polygon, the method maps the shortest path distance from the apex to all observation points, taking obstacles into account. We then fit a quadratic function to the resulting elevation-distance data pairs, processed using a median filter. For synthetic fan surfaces produced by the forward algorithm, we check that the inverse method precisely recovers the assumed elevation-distance curve, to within numerical error. We then extract empirical relations between elevation and shortest path distance from actual fan surfaces in Italy and Taiwan, and

---

*f09521304@ntu.edu.tw
†tzuyinchen@ntu.edu.tw
‡Corresponding author: hcapart@yahoo.com

show that they provide a better approximation of fan topography than the relations between elevation and direct distance assumed in previous works.

Keywords: Debris flow; Alluvial fan; Fan profile; Morphometry; Computational geometry; Shortest path map

CRediT authorship contribution statement

Yuan-Hung Damiel Chiu: Conceptualization, Data curation, Formal analysis, Investigation, Methodology, Software, Validation, Visualization, Writing - original draft. **Tzu-Yin Kasha Chen:** Supervision, Validation, Writing - review & editing. **Hervé Capart:** Conceptualization, Funding acquisition, Investigation, Methodology, Supervision, Validation, Visualization, Writing - review & editing.

1 Introduction

At tributary confluences and along mountain fronts, debris flows and fluvial transport often build up conical sediment deposits. These debris and alluvial fans are of interest as sedimentary records (Harvey, 2012; Nicovich et al., 2023), and because of the hazards they pose to people and infrastructure (Davies and McSaveney, 2008; Calvo and Savi, 2009; Khan et al., 2013). In particular, fans may aggrade rapidly due to episodic debris flows and floods. (Blair and McPherson, 2009; Hsieh and Capart, 2013; de Haas et al., 2018). It is then important to predict the resulting aggradation heights and affected areas.

Methods to delineate hazard areas range from simple travel-distance estimates (Rickenmann, 2005) to detailed analyses using numerical flow simulations. Such simulations (e.g. Hsu et al., 2010; Wu et al., 2013; Yanagisaki et al., 2016; Shiu et al., 2023) can accommodate complex terrain, and involve detailed computations of velocities and depth during flow. These models, however, are computationally expensive and difficult to calibrate from limited field data. We propose here a simpler, geometry-based method that can be calibrated directly from fan topography. The method assumes that flow proceeds down paths of steepest descent, and produces deposits characterized by a consistent distance-elevation relationship. The resulting geometry depends on whether fans are confined or unconfined (Stanistreet and McCarthy, 1993; Al-Farraj and Harvey, 2005). Whereas unconfined fans spread freely across open terrain, confined fans, on the other hand, are constrained by the surrounding topography.

For unconfined fans, flow occurs down unobstructed, straight paths that radiate from the apex. The profile of elevation versus radial distance then uniquely determines the geometry of the deposit. Typically, this profile is concave upwards, featuring slopes that decrease with distance (Bull, 1977; Bowman, 2019). Such profiles are straightforward to deduce from field data, by plotting elevations against the direct distance from the apex (Bull, 1964; Nicovich et al., 2023; Iacobucci et al., 2024). Exponential and quadratic fits can then be used to approximate empirical profiles (Troeh, 1965; Rice and Church, 2001). Various theoretical models based on hydraulic or diffusive principles have also yielded profile shapes (Parker et al., 1998; De Chant et al., 1999; Densmore et al., 2007; De Chant et al., 2021).

For confined fans, the geometry becomes more complex. Flows still take place down paths of steepest descent, but these paths must now bend around topographic obstacles. The resulting deposits are no longer radially symmetric. Nevertheless, it is still possible to define an elevation-distance profile, provided that the distance is measured along the bent flow paths. In Chen and Capart (2022), we proposed an algorithm to reconstruct confined fan surfaces from an assumed elevation-distance profile. The resulting surfaces were found to be in good agreement with the surveyed topography of various complex fans. However, identifying the elevation-distance profile from surveyed data remained unresolved. In this paper, we consider this inverse problem, complementary to the forward problem addressed in Chen and Capart (2022).

The paper is structured as follows: the methodology is presented in Section 2. In Section 3, the inverse and forward methods are demonstrated on a proof-of-concept case. To check the accuracy of the inverse method, it is applied in Section 4 to multiple fans in Italy and Taiwan. Their morphometric analysis is presented in Section 5, before conclusions in Section 6.

2 Methodology

2.1 Assumptions and forward model

Figure 1 illustrates the physical and geometrical assumptions of our method. Considering first an idealized sand pile without any obstacles (Fig. 1a), sand grains supplied at apex A flow down paths of steepest descent, and form a cone-shaped deposit of inclination set by the angle of repose θ. Given this angle of repose, an initial topography (here a flat plane), and an apex of given position and elevation, we can deduce the topography of the sand pile

$$z(x, y) = z_A - \tan\theta \, s(x, y) \,, \tag{1}$$

where $s(x, y)$ is the direct horizontal distance from apex A given here by

$$s(x, y) = \sqrt{(x - x_A)^2 + (y - y_A)^2} \,. \tag{2}$$

This represents a circular cone, or surface of revolution with a straight generatrix γ (red line). The intersection of this cone with the underlying initial flat plane also defines the boundary $\mathcal{B}$ (blue line) of the pile. For debris and alluvial fans (Fig. 1b), we assume that transport likewise proceeds down paths of steepest descent, but now the deposit slope decreases with the horizontal distance from the apex. Over a flat plane, the resulting unconfined fan deposit becomes a surface of revolution with a curved generatrix γ (red curve). The topography of the fan is given by:

$$z(x, y) = F(s(x, y)) \,, \tag{3}$$

where $F(s)$ is a generic function describing the elevation-distance profile. Given this relationship $z = F(s)$, we can determine both the fan's surface topography $z(x, y)$ and its boundary $\mathcal{B}$, where the fan deposit meets the initial flat plane.

With obstacles present (Fig. 1c), flow paths must bend, for instance at the corner C to reach point D. For confined debris and alluvial fans (Fig. 1d), the generatrix γ has a curved profile, hence the elevation contours are no longer evenly spaced. Orthogonal to these contours, the steepest path segments nevertheless remain straight in plan between turning points, just like the corresponding path segments of the constant slope sand pile of Fig. 1c. The elevation at point D continues to satisfy $z_D = F(s_D)$, but now s_D must account for the path around obstacles:

$$s_D = \sqrt{(x_C - x_A)^2 + (y_C - y_A)^2} + \sqrt{(x_D - x_C)^2 + (y_D - y_C)^2}\,. \tag{4}$$

The travel distance is therefore not the direct distance AD but the *shortest path distance* along path ACD. Although calculations become more complex, the fan deposit topography and boundary produced in the presence of obstacles can again be fully determined once the following data are provided: the initial terrain and geometry of the obstacle, the position and elevation of the apex A, and the elevation-distance function $z = F(s)$. Moreover, this remains true even for fans that form over irregular, three-dimensional terrain, featuring paths that may need to bend repeatedly around valley sides and other obstacles.

To solve this *forward problem*, a general iterative algorithm was proposed and demonstrated by Chen and Capart (2022). This method uses a 2D visibility polygon algorithm (Ghosh, 2007; Obermeyer et al., 2008) to generate fan sectors from an initial apex. It then identifies corners that act as new children apexes, repeating the process until the full fan surface is constructed. The outer boundary $\mathcal{B}$ of the fan deposit is also obtained as part of the solution. Within and along this boundary, the final fan surface $z(x, y)$ produced by the iterative procedure satisfies the eikonal equation,

$$|\nabla z(x, y)| = S(s(x, y))\,, \tag{5}$$

where ∇ is the gradient and $S = -dz/ds = -dF/ds$ denotes the distance-dependent slope. Full details regarding the forward algorithm are provided in Chen and Capart (2022). An implementation is also included in the code repository described in the computer code availability section. Applications of the eikonal equation to sand piles and natural landscapes have also been proposed by Pauli and Gioia (2007) and Anand et al. (2023).

To illustrate the forward method, consider the idealized example shown in Fig. 2a,b. The initial topography (in gray) is an inclined front plane connecting two flat horizontal regions, into which a prismatic V-shaped canyon is incised. An apex is placed within the canyon (green point), and a curved elevation-distance profile is given (red line). Given these data, the forward algorithm produces the resulting fan surface (in brown) and its outer boundary $\mathcal{B}$. The fan is partly confined within the canyon, before spreading out down the inclined plane and over the horizontal plain. The outer boundary $\mathcal{B}$ features lateral margins where the fan connects with steeper topography (canyon sides and front plane) and a fan toe where the fan onlaps milder topography (the horizontal plain). Given this boundary $\mathcal{B}$, we observe that we could replace it with a vertical wall without altering the resulting fan surface (Fig. 2c).

2.2 Proposed inverse method and validation

Complementing the forward algorithm described in the previous section, this paper addresses the *inverse problem* of retrieving the elevation-distance profile from the topography of a fan. Given a fan surface $z(x, y)$, apex A, and boundary $\mathcal{B}$, the goal is first to compute the shortest path distance $s(x, y)$ from the apex A to any point within and along boundary $\mathcal{B}$. The resulting 2D distance map is the Shortest Path Map (SPM). Once the SPM is generated, the elevation-distance data pairs (s, z) can be used to establish the fan's characteristic profile $z = F(s)$.

To compute the shortest path distance $s(x, y)$ from apex A, constrained by the boundary $\mathcal{B}$, we could use an iterative version of the 2D visibility polygon algorithm. This method has been used by various authors (Lee and Preparata, 1984; Kapoor and Maheshwari, 1988; Berg et al., 2008) for optimal path planning in 2D geometries with obstacles. Here we choose instead to specialize the algorithm of Chen and Capart (2022). The equation that must be satisfied by the shortest path distance $s(x, y)$ is given by

$$|\nabla s(x, y)| = 1\,, \tag{6}$$

with condition $s = 0$ at apex A and constrained by boundary $\mathcal{B}$. This is a special case of Eq. (5), obtained by setting the slope $S = 1$ corresponding to a 45° inclination. The boundary constraint $\mathcal{B}$ is modeled as a vertical wall by constructing an artificial topography with zero elevation within $\mathcal{B}$ and a high elevation (z_{wall}) set to ten times the domain diagonal outside it. The apex height is set to $z_A = z_{\text{wall}}$. The shortest path distance $s(x, y)$ can then be deduced by applying the forward algorithm to this special geometry. Using Chen and Capart (2022)'s fan simulation tool with $S = 1$ and apex at $(x_A, y_A, z_{\text{wall}})$, we generate solution $z(x, y)$ descending from z_{wall} within $\mathcal{B}$. The resulting elevation drop on this artificial surface, $z_{\text{wall}} - z(x, y)$, directly yields the shortest path distance $s(x, y)$, as shown in Fig. 2d. This approach efficiently computes the SPM for confined fan geometries.

As illustrated by Fig. 3, the shortest path distance s differs significantly from the direct Euclidean distance d used in previous studies (Staley et al., 2006; Cavalli and Marchi, 2008; Hamilton et al., 2013). While d represents straight-line distances that can unphysically cross obstacles (Fig. 3a), s accounts for the bent paths caused by boundary constraints (Fig. 3b). As a result, the (d, z) data pairs (black dots, Fig. 3c) scatter away from the correct elevation-distance relationship (red line), but the (s, z) data pairs (black dots, Fig. 3d) collapse precisely onto the correct relation. This demonstrates that the shortest path method is an accurate inverse of the forward algorithm.

2.3 Field case application procedure

Applying the inverse method to field cases involves three main steps: (1) Delineating the fan boundary $\mathcal{B}$, (2) Generating the SPM based on $\mathcal{B}$, and (3) Fitting a quadratic function to the elevation-distance data. While SPM generation was described in Section 2.2, this section details the boundary delineation and quadratic fitting steps. We demonstrate the procedure on the Putunpunas fan in the Laonong river valley, Taiwan (Fig. 4, 5). This fan has repeatedly aggraded due to strong debris flows exiting from its steep catchment. We analyzed this fan using a digital elevation model (DEM) from January 2014, following a significant debris-flow event in June 2012 (Hsieh and Capart, 2013). The DEM and aerial photo were provided by CECI Engineering Consultants, Inc., Taiwan.

2.3.1 Delineating the fan boundary $\mathcal{B}$

$\mathcal{B}$ is delineated using DEMs and imagery data. Hillshade maps and contour lines derived from DEMs illustrate fan morphology: contour lines in alluvial fans are more widely spaced than in mountains but closer than in riverbeds, forming characteristic outward-radiating patterns from the valley mouth. Following Moore and Howard (2005), we identify the fan's upper boundary where contour lines transition from concave to convex planimetric form downstream, and trace the continuous deposit to the fan toe (Fig. 4a).

Satellite imagery and aerial photography complement topographic analysis by revealing distinct colors and textures of fan deposits (Fig. 4b). In transitional zones, we conservatively drew boundaries to exclude ambiguous areas, ensuring accurate representation of the fan surface.

For fans with interior obstacles, such as the Putunpunas fan (Fig. 4b), interior boundaries must also be delineated. These obstacles, typically older terrace deposits or bedrock exposures, influence sediment transport paths and depositional patterns. Including these internal boundaries provides a more precise representation of the fan's morphological characteristics. The boundaries of internal obstacles are treated as vertical walls, just like the outer walls illustrated in Fig. 2.

2.3.2 Generating the Shortest Path Map (SPM) based on $\mathcal{B}$

To calculate distances, the apex is by default the point of maximum elevation within the boundary. An analyst may override this default choice by selecting a different location, along or within the fan boundary. This may be needed, for instance, if the upstream reaches of the fan have been affected by channel incision.

We then compute and compare two distance metrics: the direct distance, which measures straight-line distances from the apex to points within the convex hull of the exterior boundary (Fig. 4c), and the shortest path distance, computed using the SPM methodology detailed in Section 2.2.

For the Putunpunas fan, the shortest path calculation must consider both exterior and interior obstacles. Unlike direct distance paths, which cross obstacles, the shortest path correctly bends around them (red line in Fig. 4c, e). Using either method, distance-elevation data pairs can be obtained for all interior points of the DEM within boundary $\mathcal{B}$. Alternatively, data pairs can also be sampled along boundary $\mathcal{B}$ at intervals equal to the DEM resolution.

The distance-elevation data pairs obtained using either the direct distance d or the shortest path distance s are illustrated on Fig. 5a,b. Figure 5a shows the results obtained by plotting (d, z) data pairs. In the fan's distal zone ($d = 2000$ to 2500 m), the data show significant scatter. This indicates that the direct distance poorly captures the actual flow paths, affected by valley confinement. By contrast, Fig. 5b shows the results obtained by plotting (s, z) data pairs. By taking into account the longer paths needed to bend around obstacles, the data spread over a longer horizontal distance range. In the distal zone ($s = 2000$ to 3000 m), scatter is considerably reduced. This shows that the shortest path distance accounts much better for the observed elevation changes. Furthermore, shortest path distance contours (Fig. 4e) align much better with the surveyed fan topography (Fig. 4a) than direct distance contours (Fig. 4c) do.

Figure 5c shows the profile obtained by sampling (s, z) data pairs along the boundary only. Although this reduces the data coverage, the resulting profile closely matches that from the full fan data (Fig. 5b). For confined fans, boundary data alone may thus suffice to reconstruct a reliable elevation-distance profile. This can be useful when a post-event DEM is not available: the perimeter can be obtained from 2D imagery only (e.g. satellite images) and used to interpolate elevations along the boundary from a pre-event DEM.

2.3.3 Fitting a quadratic function to the elevation-distance relationship

Although using the shortest path distance significantly reduces scatter, the (s, z) data pairs still exhibit some dispersion. This residual scatter may be due to interactions between primary depositional and secondary modification processes (Blair and McPherson, 1994b), including incision (Vincent et al., 2022), local topographic variations, and slope variations across different azimuthal directions (Le Hooke and Rohrer, 1979), that make the fan surface more complex than assumed by our model. To address this variability, we apply two processing steps. The first step uses median filtering: we partition the distance domain between fan apex ($s_A = 0$) and toe ($s_T = \max(s_i)$) into 50 equal-sized bins, calculating median elevations to minimize local topographic effects (black dots in Fig. 5a, b). When only boundary data are used (Fig. 5c), the median filter is not needed. Following Troeh (1965), the second step is to use least squares to fit the filtered data by a quadratic function. This choice of a quadratic profile is supported by numerous previous studies (Bull, 1977; Le Hooke and Rohrer, 1979; Nanninga and Wasson, 1985; De Chant et al., 1999; Rice and Church, 2001; De Chant et al., 2021) across diverse geological settings. However, extrapolating the quadratic curve beyond observed data points may yield unrealistic results. To better represent fan morphology, we adopt a piecewise function with the fan apex at $s = s_A = 0$. The function combines a quadratic fit within the fan body $0 < s < s_T$ with linear extrapolation at both ends: a constant slope matching the channel gradient upstream $s \leq 0$ and a tangent line downstream $s \geq s_T$. This formulation prevents unrealistic slope reversals that might occur with a simple quadratic extrapolation while ensuring smooth transitions at boundaries. Moreover, the linear segments better capture the characteristic steepening of slopes at both channel-fan and fan-floodplain transitions. The assumed elevation-distance profile is therefore defined by:

$$\hat{z}(s) = \begin{cases} \hat{S}s + \hat{P}, & s \leq 0\,, \\ \hat{L}s^2 + \hat{S}s + \hat{P}, & 0 < s < s_T\,, \\ (2\hat{L}s_T + \hat{S})s - \hat{L}s_T^2 + \hat{P}, & s \geq s_T\,, \end{cases} \tag{7}$$

where $\hat{L}$ controls profile concavity or convexity, while $\hat{S}$ and $\hat{P}$ represent the slope and elevation at the fan apex ($s = 0$).

In Fig. 5a-c, the fitting lines are plotted together with the original distance-elevation data. Overall, the data are fitted well by the assumed quadratic profiles. The quality of the fit, however, is comparatively poorer at the distal end of the fan, where the topography transitions to the milder sloped trunk river bed.

2.3.4 Evaluating model performance

We evaluate the inverse method with two complementary metrics: the Root Mean Squared Error (RMSE) to assess the profile fit, and a Difference of DEMs (DoD) to assess the spatial accuracy of the resulting idealized surface.

First, the RMSE is the differences between the raw elevation data and the elevations deduced from the quadratic fit. This value allows for effective comparison of different distance metrics (e.g., direct vs. shortest path), with a lower RMSE indicating a better fit. For the fan shown in Fig. 4 and Fig. 5, the RMSE results clearly show the superiority of the shortest path distance method. The new method reduces the profile's RMSE by over 3× (from 13.44 m to 4.23 m) when compared to using direct distance.

This result allows for a nuanced interpretation of the model's performance. The significant reduction in RMSE quantifies the correction of a major model formulation error: the flawed assumption that transport paths are straight. With this systematic bias addressed, the final residual RMSE is best understood as a composite measure. It reflects both the fan's true geomorphic complexity, including its physical deviation from an ideal shape due to processes such as backstepping or channelization, and the inherent limitations of the model's isotropic assumption, which remain even after adopting the improved distance metric.

Second, to assess how well the idealized isotropic fan model represents the actual fan surface, we compute a DoD. For each distance metric being tested, an idealized fan surface is first constructed by applying the fitted quadratic profile (Eq. 7) to the corresponding distance map. This idealized surface is then subtracted from the actual fan topography to produce a map of model residuals (Fig. 4d,f). This spatial analysis allows for a more direct visual and quantitative comparison of different methods, as demonstrated for the Putunpunas fan, where the shortest path method significantly reduces the magnitude of the residuals. Crucially, these residuals are more than just a measure of error; they reveal where the fan's true morphology deviates from the idealized model, often highlighting the influence of secondary geomorphic processes like channel incision or asymmetric anisotropic deposition.

2.4 Application to a large-scale, fluvially-dominated fan

To check that our method is suitable regardless of scale and formative process, we also applied it to the Laonong River fan, Taiwan, a fluvially-dominated system 200 times larger (128 km^2) than the Putunpunas fan. For this application, we followed the same procedure detailed in Section 2.3, with one key modification: to isolate the primary fan topography, we excluded the active river channel using boundaries from Taiwan's Water Resources Agency (WRA) (Fig. 6a,b).

At this larger scale, the shortest path distance again proved superior to the direct distance. Its distance contours align more closely with the observed elevation contours, especially in the northern portion of the fan (Fig. 6c,e). The resulting elevation-distance data pairs (Fig. 7b) exhibit significantly less scatter and a lower RMSE than the data pairs derived from direct distance (Fig. 7a). Quantitatively, the shortest path method nearly halved the profile's RMSE from 4.83 m to 2.63 m and reduced elevation discrepancies in the reconstructed surface by up to 10 m compared to the direct distance model (Fig. 6d,f).

This large-scale application demonstrates the method's robustness, including its ability to identify geomorphic processes, as the DoD map (Fig. 6f) clearly delineates areas of significant river incision. In addition, the method provided a quantitative basis for refining the fan boundary. Given the ambiguous apex location, we tested several candidate delineations and selected the one that minimized the profile's RMSE, yielding a result consistent with previous geomorphic studies (Lin et al., 2009).

3 Fan surface reconstruction test

This section tests our method's ability to reconstruct a complete fan surface from partial survey data. We focus on a single depositional event, for which data are unusually complete. It is therefore possible to rigorously test the complete inverse-forward workflow.

The chosen case is a fan aggradation event on 7 August 2021, at the confluence of Taiwan's Laonong River and its Yu-Shui tributary. A single debris flow from the Yu-Shui catchment deposited approximately 3 million m^3 of debris, causing aggradation of 20 m or more over an area of 65000 m^2. The unusually complete pre- and post-event dataset for this event (Table 1) provides a unique validation opportunity. We derived the elevation-distance profile from a later post-event DTM, excluding areas modified by subsequent excavation work. This profile was then used in the forward model to reconstruct the complete fan surface. The reconstruction can then be validated against survey data acquired immediately (five days) after the event, allowing comparison between the fan reconstructed from partial data and the actual fan surface.

Table 1: Summary of datasets used for Yu-Shui fan reconstruction analysis

Data Type	**Resolution**	**Date**	**Source**	**Description**
Lidar DTM	10 m	June 2016	Ministry of the Interior (MOI), Taiwan	Pre-event terrain conditions
SPOT Satellite Imagery	1.5 m	February 1, 2021	Center for Space and Remote Sensing Research, NCU	Pre-event surface conditions
Aerial Photography & DSM	0.18 m / 0.7 m	August 12, 2021	National Science and Technology Center for Disaster Reduction (NCDR)	Immediate post-event documentation
SPOT Satellite Imagery	1.5 m	November 7, 2021	Center for Space and Remote Sensing Research, NCU	Later post-event surface conditions
Lidar DTM	10 m	January 2022	CECI Engineering Consultants	Later post-event terrain conditions

The analysis steps are shown in Fig. 8. For the inverse method (Fig. 8a,d), we used the later post-event DTM and imagery to delineate the fan boundary and identify excavated areas. After excluding these modified areas, we derived the elevation-distance profile using median filtering and quadratic fitting (Fig. 8c,d). As previously found, the shortest path data pairs (s, z) are well fitted by the quadratic profile, and show significantly less scatter (RMSE = 2.48 m; Fig. 8d) than the direct distance data pairs (d, z) (RMSE = 7.67 m; Fig. 8c)

Next, we used the forward method to reconstruct the fan surface (Fig. 8e) from three inputs: the fitted elevation-distance function, the apex location, and an initial topography (z_{init}). To model aggradation only, this initial topography was a composite of minimum elevations from pre- and later post-event DTMs (Fig. 8b). Within the fan's final footprint, 91.4% of this surface was from the pre-event DTM. The apex location (x_A, y_A) was aligned with the inverse method's apex point, with z_A derived from the fitted elevation-distance curve at $s = 0$ ($z_A = \hat{P}$) to maintain consistency between input parameters and reconstructed morphology.

Figure 8e shows the reconstructed fan surface and associated deposit thickness $z - z_{\text{init}}$ ranging from 0 to 30 m. Figure 8f then maps the difference Δz between the reconstructed surface and the immediate post-event topography, used as validation data. Although the reconstructed surface slightly overestimates the fan elevation along the inner bank of the bend, good overall agreement is observed.

Further comparisons between the reconstructed fan elevations and those used for calibration and validation are provided by the scatter plots of Fig. 9a,b. On both plots, the data cluster closely along the line of perfect agreement. The model achieved an RMSE of 3.09 m against the calibration data and a comparable 3.45 m against the validation data.

The results demonstrate our methodology's capabilities and limitations. A key strength is that the reconstructed surface successfully reproduces the complete fan surface and extent (Fig. 8e), despite being calibrated with partial data. This validates our morphological assumptions in data-deficient regions. The method, however, is subject to two important limitations. First, it can only model aggradation, and does not capture the erosion that took place along the bank opposite the fan. A second limitation is that our approach does not determine how the apex location or elevation will respond to future events. For future hazard assessments, this uncertainty must be taken into account, for instance, by considering multiple scenarios for the post-event apex location and elevation.

4 Application to multiple fans

This section evaluates the effectiveness of the shortest path distance approach by applying it to multiple fans. We consider two contrasting regional datasets: an analysis of 25 fans from the alpine setting of Italy's Valtellina Valley and a study of 50 large-scale (> 2 km^2) alluvial fans in Taiwan. Following these applications, we perform a comparative assessment of the three profile extraction methods to quantitatively evaluate their accuracy and provide practical guidelines for their application.

4.1 Fans in Valtellina Valley, Italy

To evaluate our method in a different environmental setting, we first analyzed alluvial fans in Italy's Valtellina Valley. The area's continental climate (1200 mm annual rainfall) (Luino et al., 2020) contrasts with Taiwan's subtropical monsoon climate ($>$2000 mm). These distinct climatic regimes, combined with different geological settings, produce markedly different fan morphologies: the Valtellina Valley fans are predominantly smaller and steeper than their Taiwanese counterparts. This alpine valley is drained by the Adda River, and the studied fans are located at the confluences of its tributaries, grading down to the main valley floor. The analysis used the AW3D30 DEM (30-meter resolution) from the Japan Aerospace Exploration Agency (JAXA). We refined the fan boundaries from Norini et al. (2016) by excluding main river valleys, separating merged fans, and removing small fans (< 0.1 km^2) to prevent spurious results, yielding a final set of 25 fans for analysis (Fig. 10a).

The elevation-distance relationships for these fans were analyzed using the inverse method, with results presented in Fig. 10b. The profiles show median elevations in 50 equal-sized bins fitted with quadratic curves (black lines). The profiles are displayed with

10× vertical exaggeration. For context, the longitudinal profile of the Adda River, which serves as the local base level for these fans, is included as a black line.

To gain a deeper understanding of these morphometric variations, we label the fans based on their dominant formative processes. Based on the work of Blair and McPherson (1994a), Crosta and Frattini (2004) used a combination of field analysis of landforms (e.g., lobes and levees), sedimentary deposits, and historical flood documentation to classify fans into Type I and Type II. In this framework, Type I fans are dominated by sediment-gravity flows (debris flows), while Type II fans are shaped by fluid-gravity flows (e.g., sheet-floods). This process-based distinction is visualized using distinct colors in Fig. 10.

In our study area (Fig. 10a), Crosta and Frattini (2004) identified three Type I (shown in red) and nine Type II fans (shown in blue). The corresponding profiles (Fig. 10b) differ mainly in terms of slope. We found that the mean slope of the Type I fans is 0.151 m/m, significantly steeper than the mean slope of 0.0985 m/m for the Type II fans. In contrast, the profile concavity, measured by the dimensionless drop (a metric defined in Section 5.1), was more similar between the groups (mean of 0.019 for Type I versus 0.0151 for Type II). This finding, which quantitatively links steeper gradients to debris-flow processes, is consistent with the general observations of Crosta and Frattini (2004).

4.2 Fans in Taiwan

To investigate regional variations and validate our methodology at a broader spatial scale, we also conducted a morphological analysis of Taiwan's major alluvial fans. Starting with the alluvial fans (area > 2 km^2) documented in Lin et al. (2009), we refined the selection using elevation contour patterns from the 20-meter resolution DEM (2016-2024 merged dataset) provided by the MOI of Taiwan. After excluding five fans whose contour patterns did not exhibit typical fan morphology, our final analysis included 50 fans, numbered from northwest to southeast (Fig. 11a). For context, Fig. 11a includes a red box showing the Putunpunas fan, the smaller debris fan considered earlier (Fig. 4)

Figure 11b presents the 50 alluvial fan profiles using a consistent color scheme. To facilitate profile comparison, we applied horizontal scaling and translation using the formula $x_T + \lambda(s_T - s)$, where x_T (fan toe position) serves as the translation baseline. The horizontal scaling coefficient λ was set to 2 for western fans and -2 for eastern fans. Each point represents the median elevation in 50 equal-sized bins, with black lines showing quadratic curve fits.

The alluvial fans display distinct regional characteristics, which can be strongly linked to their terminal boundary conditions. To investigate this, we classified the 50 fans as either "distally unconfined" (terminating on open plains) or "distally confined" (terminating in constricted valleys). This classification aligns with Taiwan's geography and explains the observed morphological differences. The western fans are predominantly distally unconfined, allowing for the development of longer fans with gentle slopes of approximately 0.5 degrees (≈0.0087 m/m). In contrast, the eastern fans are almost all distally confined by the narrow coastal plain between the Central and Hai'an mountain ranges. This spatial constraint results in significantly steeper fans, with slopes typically ranging from 3 to 6 degrees (≈0.0524 to 0.1051 m/m). These quantitative relationships between confinement and fan morphometry are further explored in our detailed analysis in Section 5.

4.3 Comparative assessment of fan profile reconstruction methods

Our analysis investigated three methodologies for characterizing alluvial fan profiles, as detailed in Section 2.3.2. We quantified performance using RMSE between fitted curves and observed elevations: direct distance (RMSE_d), interior shortest path (RMSE_s), and boundary shortest path (RMSE_b). The analysis, applied to the Putunpunas fan, the Yu-Shui fan, 50 larger Taiwanese fans including the Laonong River fan, and 25 Italian fans, used RMSE_s as reference due to its consistent performance. To quantify boundary complexity, we used a dimensionless compactness index (P_c/P_b), where P_c is the convex hull perimeter (dashed line in Fig. 4c) and P_b is the fan boundary perimeter (black outline in Fig. 4e).

As shown by Fig. 12a, the RMSE between the elevation-distance profile and the original data pairs can be reduced significantly by using the shortest path distance instead of the direct distance. Results show that their relative performance depends strongly on fan planform. For unconfined fans (P_c/P_b approaching 1), the shortest path method performs similarly to the direct distance method, as could be expected. In confined settings with irregular boundaries, however, the shortest path method performs significantly better than the direct distance method. The corresponding error, RMSE_s, is reduced by up to 3.5 times compared to the direct distance method error, RMSE_d. Over all 77 fans, the shortest path method performs equivalently or significantly better than the direct distance method, demonstrating its ability to accurately capture fan morphology regardless of whether obstacles are present.

As shown by Fig. 12b, using boundary measurements alone generally produces larger errors than using data from the entire fan. The error for boundary-based measurements, (RMSE_b, is on average 1.25 times greater than the error for full fan measurements, RMSE_s), independent of fan morphology. However, accuracy comparable to interior methods can be attained when using high-resolution data (1 and 5 m). This improvement in boundary method performance is attributed to the enhanced precision in boundary delineation afforded by high-resolution topographic data, as demonstrated by the Putunpunas and Yu-Shui cases.

These findings provide practical guidelines: shortest path methods should be preferred when $P_c/P_b < 0.8$, boundary-based measurements require high-resolution data, and the P_c/P_b ratio can predict potential errors in direct distance measurements. These insights provide a framework for selecting measurement approaches based on fan morphology and data quality, with potential applications in quantifying systematic errors within existing databases. Note also that the RMSE_s for the shortest path method should not be interpreted as a model failure, but rather as a substantially improved indicator of geomorphic complexity. They quantify the extent to which a real-world fan, whether formed by debris flows or fluvial processes, deviates from the idealized geometric solid constructed by our method.

5 Morphometric analysis

This section performs a detailed morphometric analysis of the full fan dataset. Using the validated shortest path distance method, we now investigate the quantitative relationships between fundamental morphological parameters, including fan area, slope, and profile concavity. The aim of this systematic analysis is to provide new insights into the morphometric patterns of alluvial fans by linking them to controlling factors such as formative processes and terminal boundary conditions across diverse geographical settings.

5.1 Morphometric indicators definitions

The morphometric characteristics of debris and alluvial fans, particularly their longitudinal slope and profile concavity, serve as fundamental parameters for understanding fan evolution (Troeh, 1965; Moore and Howard, 2005; Williams et al., 2006). Various key characteristics can be deduced from the fitted profiles defined by Eq. (7). The first is total fan relief, or the total elevation difference $\Delta\hat{z} = \hat{z}_A - \hat{z}_T$. This can be obtained from Eq. (7) as

$$\Delta\hat{z} = \hat{z}(0) - \hat{z}(s_T) = -\hat{L}s_T^2 - \hat{S}s_T\,. \tag{8}$$

A second characteristic is the mean fan slope $\Delta\hat{z}/s_T$, which also equals the local slope at the midpoint:

$$\frac{\Delta\hat{z}}{s_T} = -\hat{L}s_T - \hat{S} = -\frac{d\hat{z}}{ds}(s_T/2)\,. \tag{9}$$

To quantify departure from constant slope, we further define the drop $\delta\hat{z}$ as the difference between a linear profile and the fitted profile at its midpoint:

$$\delta\hat{z} = \frac{\hat{z}_A + \hat{z}_T}{2} - \hat{z}(s_T/2) = \frac{1}{4}\hat{L}s_T^2\,. \tag{10}$$

We then make this dimensionless by normalizing with respect to the fan length s_T. The resulting dimensionless drop $\delta\hat{z}/s_T = \frac{1}{4}\hat{L}s_T$ scales linearly with the quadratic coefficient $\hat{L}$, and provides a measure of the concavity of the fan profile. It is also proportional to the slope differential between the fan's apex and toe, equal to $2\hat{L}s_T$. The variables used in the above definitions are illustrated in Fig. 2b.

5.2 Results and discussion

Analysis of the 77-fan dataset using the validated shortest path method reveals three key morphometric relationships (Fig. 13a-c). First (Fig. 13a), a strong negative correlation between fan area and slope indicates that smaller fans are systematically steeper. Second (Fig. 13b), larger fans exhibit decreased profile concavity, a trend also observed on Martian fans (Kraal et al., 2008). This relationship may reflect how smaller, more concave fans create abrupt topographic transitions between steep catchments and gentle depositional plains, whereas larger fans grade more smoothly into their surroundings. Finally (Fig. 13c), our results confirm a strong positive relationship between slope and concavity, showing that steeper fans are more concave, a finding consistent with previous work (Moore and Howard, 2005; Seybold et al., 2021).

The distribution of fans within these general trends is potentially influenced by both formative processes and terminal boundary conditions. Although the sample size for process-based classification is limited, the Italian data suggests that debris-flow dominated (Type I) fans are steeper than their fluvial (Type II) counterparts. The role of terminal conditions is more clearly demonstrated by the Taiwanese fans, where distally confined fans are steeper and more concave than unconfined fans of a similar area.

When explicitly compared to previous studies of Taiwanese fans, our regression of fan area versus slope is steeper than that found by Lin et al. (2009), likely due to our use of higher-resolution DEMs and a different regression methodology; specifically, we applied a logarithmic transformation to the data before linear regression to ensure that smaller-sloped fans were weighted equally in the analysis. The impact of our updated methodology is best illustrated by the large Choshui fan (No. 1). Despite using the same fan boundary as Lin et al. (2009), our calculated slope (0.0056 m/m) is three times gentler than their value (0.017 m/m). We confirmed this gentler slope with a direct calculation from our own high-resolution DEM. This large discrepancy is most likely attributable to Lin's use of lower-resolution 40 m DEM data from the 1980s in combination with a different slope calculation methodology. The regression analysis of Saito and Oguchi (2005), on the other hand, shows a similar slope trend to our findings but with a parallel shift, potentially due to differences in the datasets used.

The regression for the entire 77-fan dataset is steeper than the Taiwan-only analysis, a result driven by the inclusion of the steep Italian fans and highlighting inter-regional differences. These differences may be attributed to variations in factors such as basin ruggedness index (Melton ratio) or mean annual precipitation (Chou et al., 2017). However, a detailed examination of these factors is beyond the scope of the current study. Nevertheless, the demonstrated morphometric relationships provide valuable insights for hazard assessment. The systematic differences linked to controlling factors suggest that hazard scenarios must be evaluated in their specific geological and climatic contexts, and the correlation between slope and concavity can be used to estimate potential aggradation patterns better.

6 Conclusion

In this study, we developed a novel inverse method for characterizing alluvial fan morphology through shortest path distance analysis. The method generates an SPM from fan boundaries and an apex, capturing topographic constraints where direct distance fails. Validation included theoretical and field tests, showing reversibility with the forward method (Chen and Capart, 2022) on a synthetic fan and broad applicability on fans of different scales, including the small, debris-flow-dominated Putunpunas fan, and the large, fluvially-dominated Laonong River fan.

The method demonstrated significant practical utility through two major applications. First, the successful reconstruction of the Yu-Shui fan event showed how elevation-distance functions derived from post-event topography can inform forward modeling, bridging the gap between simple direct distance estimations and complex numerical simulations. Second, a broad morphometric analysis of 77 fans in Taiwan and Italy established the superior performance of the shortest path metric and revealed key controls on fan morphology. Our analysis quantitatively demonstrated that fan shape is strongly linked to terminal boundary conditions, with distally confined fans being steeper and more concave than distally unconfined fans.

Comparative analysis established the superior performance of shortest path metrics over direct distance measurements, particularly in confined settings with low boundary compactness. The method revealed key morphological relationships, including the inverse correlation between fan area and both slope and concavity. Notably, these trends match observations of Terrestrial and Martian fans (Moore and Howard, 2005; Kraal et al., 2008; Seybold et al., 2021), suggesting universal mechanisms in fan formation processes across different planetary environments. The ability of our method to capture these consistent trends across vastly different scales underscores its fundamental strength: it is built upon scale-invariant geometric principles. The concept of using a shortest path distance map and fitting an elevation-distance profile is not dependent on the absolute size of the fan but rather on its overall geometric form.

Various avenues are suggested for further work. First, the shortest path distance could be used to analyze other properties of debris and alluvial fans than just their elevation profiles. These could include surface roughness (e.g. Cavalli and Marchi, 2008) and grain size variations (e.g. Reynolds, 2024). Secondly, the geometric fan characteristics exploited by our method could be used for other tasks, including automated fan delineation (see e.g. Iacobucci et al., 2024) or the reconstruction of ancient fan surfaces from preserved terrace deposits (see e.g. Chen et al., 2022). Finally, our proposed method could be used to map aggradation risk, by simulating a variety of possible future fan surfaces under various scenarios.

7 Acknowledgments

The early development of the proposed method was pursued while Y.-H. D. Chiu and H. Capart were on a research stay in Louvain-la-Neuve kindly hosted by Prof. Sandra Soares-Frazão (UCLouvain) and Dr. B. Spinewine (Fugro Engineers). We also thank the developers of key algorithms used in this study. The visibility polygon algorithm was implemented using the Python binding of VisiLibity1 (Obermeyer et al., 2008) and was modified to record children apexes. Contour extraction was performed using scikit-image (Van Der Walt et al., 2014). We acknowledge Darren Engwirda for developing the point-in-polygon algorithm, as described in Kepner et al. (2020), and thank Hans Alemão for maintaining the easily installable version. Guidance regarding the GitHub platform was kindly provided by Colin Stark. This research was funded by the National Science and Technology Council (NSTC), Taiwan (Grant No. NSTC111-2221-E-002-058-MY3). Additional support and fruitful feedback from the CECI Engineering Consultants Geotechnical Team led by Associate Manager Chia-Hsin Chang are gratefully acknowledged.

8 Computer code availability

Library Name: fan-inverse-forward-methods

License: LGPL-3.0

Year First Available: 2025

Hardware Required: Any standard personal computer (Tested in Windows)

Software Required: Python 3.11 or later with GDAL, inpoly-cython, Matplotlib, NumPy, SciPy, Shapely, scikit-image, tqdm, and a modified VisiLibity.

Program Language: Python

Program Size: 48 MB total (includes 42 MB for GDAL wheel package)

Source Code Access: Available at GitHub: https://github.com/damiel-hub/fan-inverse-forward-methods. Documentation and installation instructions included in README.

9 Declaration of generative AI in scientific writing

During the preparation of this work, the first author used Gemini, ChatGPT and Claude to assist with grammar and sentence readability in the initial draft, as well as to help translate MATLAB code to Python code and assist with code formatting and comments.

After using these tools, the authors comprehensively reviewed and edited the content and take full responsibility for the content of the publication.

References

Al-Farraj, A., Harvey, A.M., 2005. Morphometry and depositional style of Late Pleistocene alluvial fans: Wadi Al-Bih, northern UAE and Oman, in: Harvey, A.M., Mather, A.E., Stokes, M. (Eds.), Alluvial Fans: Geomorphology, Sedimentology, Dynamics. Geological Society of London. volume 251, p. 0. URL: `https://doi.org/10.1144/GSL.SP.2005.251.01.07`, doi:`10.1144/GSL.SP.2005.251.01.07`.

Anand, S.K., Bertagni, M.B., Singh, A., Porporato, A., 2023. Eikonal Equation Reproduces Natural Landscapes With Threshold Hillslopes. Geophysical Research Letters 50, e2023GL105710. URL: `https://agupubs.onlinelibrary.wiley.com/doi/abs/10.1029/2023GL105710`, doi:`10.1029/2023GL105710`.

Berg, M.d., Cheong, O., Kreveld, M.v., Overmars, M., 2008. Visibility Graphs, in: Computational Geometry: Algorithms and Applications. Springer Berlin Heidelberg, Berlin, Heidelberg, pp. 323–333. URL: `https://doi.org/10.1007/978-3-540-77974-2_15`, doi:`10.1007/978-3-540-77974-2_15`.

Blair, T.C., McPherson, J.G., 1994a. Alluvial Fan Processes and Forms, in: Abrahams, A.D., Parsons, A.J. (Eds.), Geomorphology of Desert Environments. Springer Netherlands, Dordrecht, pp. 354–402. URL: `https://doi.org/10.1007/978-94-015-8254-4_14`, doi:`10.1007/978-94-015-8254-4_14`.

Blair, T.C., McPherson, J.G., 1994b. Alluvial fans and their natural distinction from rivers based on morphology, hydraulic processes, sedimentary processes, and facies assemblages. Journal of Sedimentary Research 64, 450–489. URL: `https://doi.org/10.1306/D4267DDE-2B26-11D7-8648000102C1865D`, doi:`10.1306/d4267dde-2b26-11d7-8648000102c1865d`.

Blair, T.C., McPherson, J.G., 2009. Processes and Forms of Alluvial Fans, in: Parsons, A.J., Abrahams, A.D. (Eds.), Geomorphology of Desert Environments. Springer Netherlands, Dordrecht, pp. 413–467. URL: `https://doi.org/10.1007/978-1-4020-5719-9_14`, doi:`10.1007/978-1-4020-5719-9_14`.

Bowman, D., 2019. Slope Gradients, in: Principles of Alluvial Fan Morphology. Springer Netherlands, Dordrecht, pp. 25–35. URL: `https://doi.org/10.1007/978-94-024-1558-2_3`, doi:`10.1007/978-94-024-1558-2_3`.

Bull, W.B., 1964. Geomorphology of segmented alluvial fans in western Fresno County, California. Report 352E. United States Department of the Interior. URL: `https://pubs.usgs.gov/publication/pp352E`, doi:`10.3133/pp352E`.

Bull, W.B., 1977. The alluvial-fan environment. Progress in Physical Geography: Earth and Environment 1, 222–270. URL: `https://journals.sagepub.com/doi/abs/10.1177/030913337700100202`, doi:`10.1177/030913337700100202`.

Calvo, B., Savi, F., 2009. A real-world application of Monte Carlo procedure for debris flow risk assessment. Computers & Geosciences 35, 967–977. URL: `https://www.sciencedirect.com/science/article/pii/S0098300408001532`, doi:`10.1016/j.cageo.2008.04.002`.

Cavalli, M., Marchi, L., 2008. Characterisation of the surface morphology of an alpine alluvial fan using airborne LiDAR. Nat. Hazards Earth Syst. Sci. 8, 323–333. URL: `https://nhess.copernicus.org/articles/8/323/2008/`, doi:`10.5194/nhess-8-323-2008`.

Chen, C.M., Shyu, J.B.H., Tsui, H.K., Hsieh, Y.C., 2022. Preservation and transportation of large landslide deposits under decadal and millennial timescales in the Taiwan orogenic belt. Geomorphology 415, 108402. URL: `https://www.sciencedirect.com/science/article/pii/S0169555X22002951`, doi:`10.1016/j.geomorph.2022.108402`.

Chen, T.Y.K., Capart, H., 2022. Computational morphology of debris and alluvial fans on irregular terrain using the visibility polygon. Computers & Geosciences 169, 105228. URL: `https://www.sciencedirect.com/science/article/pii/S0098300422001777`, doi:`10.1016/j.cageo.2022.105228`.

Chou, H.T., Lee, C.F., Lo, C.M., 2017. The formation and evolution of a coastal alluvial fan in eastern Taiwan caused by rainfall-induced landslides. Landslides 14, 109–122. URL: `https://doi.org/10.1007/s10346-016-0678-6`, doi:`10.1007/s10346-016-0678-6`.

Crosta, G.B., Frattini, P., 2004. Controls on modern alluvial fan processes in the central Alps, northern Italy. Earth Surface Processes and Landforms 29, 267–293. URL: `https://onlinelibrary.wiley.com/doi/abs/10.1002/esp.1009`, doi:`10.1002/esp.1009`.

Davies, T.R., McSaveney, M.J., 2008. Principles of sustainable development on fans. Journal of Hydrology (New Zealand) 47, 43–65. URL: `http://www.jstor.org/stable/43944963`. publisher: New Zealand Hydrological Society.

De Chant, L.J., Pease, P.P., Tchakerian, V.P., 1999. Modelling alluvial fan morphology. Earth Surface Processes and Landforms 24, 641–652. URL: `https://onlinelibrary.wiley.com/doi/abs/10.1002/%28SICI%291096-9837%28199907%2924%3A7%3C641%3A%3AAID-ESP979%3E3.0.CO%3B2-3`, doi:`10.1002/(SICI)1096-9837(199907)24:7<641::AID-ESP979>3.0.CO;2-3`.

De Chant, L.J., Pease, P.P., Tchakerian, V.P., 2021. Alluvial fan morphology: A self-similar free boundary problem description. Geomorphology 375, 107532. URL: `https://www.sciencedirect.com/science/article/pii/S0169555X20305055`, doi:`10.1016/j.geomorph.2020.107532`.

Densmore, A.L., Allen, P.A., Simpson, G., 2007. Development and response of a coupled catchment fan system under changing tectonic and climatic forcing. Journal of Geophysical Research: Earth Surface 112. URL: `https://onlinelibrary.wiley.com/doi/abs/10.1029/2006JF000474`, doi:`10.1029/2006JF000474`.

Ghosh, S.K., 2007. Visibility Algorithms in the Plane. Cambridge University Press, Cambridge. URL: `https://www.cambridge.org/core/product/BCD82CF5FE665832FAC4AAAB68305AF1`, doi:`10.1017/CBO9780511543340`.

de Haas, T., Densmore, A., Stoffel, M., Suwa, H., Imaizumi, F., Ballesteros-Cánovas, J., Wasklewicz, T., 2018. Avulsions and the spatio-temporal evolution of debris-flow fans. Earth-Science Reviews 177, 53–75. URL: `https://www.sciencedirect.com/science/article/pii/S0012825217302465`, doi:`10.1016/j.earscirev.2017.11.007`.

Hamilton, P.B., Strom, K., Hoyal, D.C.J.D., 2013. Autogenic incision-backfilling cycles and lobe formation during the growth of alluvial fans with supercritical distributaries. Sedimentology 60, 1498–1525. URL: `https://onlinelibrary.wiley.com/doi/abs/10.1111/sed.12046`, doi:`10.1111/sed.12046`.

Harvey, A.M., 2012. The coupling status of alluvial fans and debris cones: a review and synthesis. Earth Surface Processes and Landforms 37, 64–76. URL: `https://onlinelibrary.wiley.com/doi/abs/10.1002/esp.2213`, doi:`10.1002/esp.2213`.

Hsieh, M.L., Capart, H., 2013. Late Holocene episodic river aggradation along the Lao-nong River (southwestern Taiwan): An application to the Tseng-wen Reservoir Transbasin Diversion Project. Engineering Geology 159, 83–97. URL: `https://www.sciencedirect.com/science/article/pii/S0013795213001063`, doi:`10.1016/j.enggeo.2013.03.019`.

Hsu, S.M., Chiou, L.B., Lin, G.F., Chao, C.H., Wen, H.Y., Ku, C.Y., 2010. Applications of simulation technique on debris-flow hazard zone delineation: a case study in Hualien County, Taiwan. Nat. Hazards Earth Syst. Sci. 10, 535–545. URL: `https://nhess.copernicus.org/articles/10/535/2010/`, doi:`10.5194/nhess-10-535-2010`.

Iacobucci, G., Delchiaro, M., Troiani, F., Nadali, D., 2024. Land-surface quantitative analysis for mapping and deciphering the construction processes of piedmont alluvial fans in the Anti-Lebanon Mountains. Geomorphology 453, 109148. URL: `https://www.sciencedirect.com/science/article/pii/S0169555X24000989`, doi:`10.1016/j.geomorph.2024.109148`.

Kapoor, S., Maheshwari, S.N., 1988. Efficient algorithms for Euclidean shortest path and visibility problems with polygonal obstacles, in: Proceedings of the Fourth Annual Symposium on Computational Geometry, ACM Press, Urbana-Champaign, Illinois, US. pp. 172–182. doi:`10.1145/73393.73411`.

Kepner, J., Kipf, A., Engwirda, D., Vembar, N., Jones, M., Milechin, L., Gadepally, V., Hill, C., Kraska, T., Arcand, W., Bestor, D., Bergeron, W., Byun, C., Hubbell, M., Houle, M., Kirby, A., Klein, A., Mullen, J., Prout, A., Reuther, A., Rosa, A., Samsi, S., Yee, C., Michaleas, P., 2020. Fast Mapping onto Census Blocks, in: 2020 IEEE High Performance Extreme Computing Conference (HPEC), IEEE, Waltham, MA, USA. pp. 1–8. URL: `https://ieeexplore.ieee.org/document/9286157/`, doi:`10.1109/HPEC43674.2020.9286157`.

Khan, M.A., Haneef, M., Khan, A.S., Tahirkheli, T., 2013. Debris-flow hazards on tributary junction fans, Chitral, Hindu Kush Range, northern Pakistan. Journal of Asian Earth Sciences 62, 720–733. URL: `https://www.sciencedirect.com/science/article/pii/S1367912012005111`, doi:`10.1016/j.jseaes.2012.11.025`.

Kraal, E.R., Asphaug, E., Moore, J.M., Howard, A., Bredt, A., 2008. Catalogue of large alluvial fans in martian impact craters. Icarus 194, 101–110. URL: `https://www.sciencedirect.com/science/article/pii/S0019103507004733`, doi:`10.1016/j.icarus.2007.09.028`.

Le Hooke, R.B., Rohrer, W.L., 1979. Geometry of alluvial fans: Effect of discharge and sediment size. Earth Surface Processes 4, 147–166. URL: `https://onlinelibrary.wiley.com/doi/abs/10.1002/esp.3290040205`, doi:`10.1002/esp.3290040205`.

Lee, D.T., Preparata, F.P., 1984. Euclidean shortest paths in the presence of rectilinear barriers. Networks 14, 393–410. URL: `https://onlinelibrary.wiley.com/doi/abs/10.1002/net.3230140304`, doi:`10.1002/net.3230140304`.

Lin, Z., Oguchi, T., Chen, Y.G., Saito, K., 2009. Constant-slope alluvial fans and source basins in Taiwan. Geology 37, 787–790. URL: `https://doi.org/10.1130/G25675A.1`, doi:`10.1130/g25675a.1`.

Luino, F., De Graff, J., Roccati, A., Biddoccu, M., Cirio, C.G., Faccini, F., Turconi, L., 2020. Eighty Years of Data Collected for the Determination of Rainfall Threshold Triggering Shallow Landslides and Mud-Debris Flows in the Alps. Water 12, 133. URL: `https://www.mdpi.com/2073-4441/12/1/133`.

Moore, J.M., Howard, A.D., 2005. Large alluvial fans on Mars. Journal of Geophysical Research: Planets 110. URL: `https://agupubs.onlinelibrary.wiley.com/doi/abs/10.1029/2004JE002352`, doi:`10.1029/2004JE002352`.

Nanninga, P.M., Wasson, R.J., 1985. Calculation of the volume of an alluvial fan. Journal of the International Association for Mathematical Geology 17, 53–65. URL: `https://doi.org/10.1007/BF01030367`, doi:`10.1007/BF01030367`.

Nicovich, S.R., Schmitt, J.G., Gray, H.J., Klinger, R.E., Mahan, S.A., Nicovich, S.R., Schmitt, J.G., Gray, H.J., Klinger, R.E., Mahan, S.A., 2023. Construction and Modification of Debris-Flow Alluvial Fans as Captured in the Geomorphic and Sedimentary Record: Examples from the Western Sangre de Cristo Mountains, South-Central Colorado, in: The Geological Society of America Special Paper. Geological Society of America. volume 561, p. 49. URL: `https://doi.org/10.1130/2023.2561(01)`, doi:`10.1130/2023.2561(01)`.

Norini, G., Zuluaga, M.C., Ortiz, I.J., Aquino, D.T., Lagmay, A.M.F., 2016. Delineation of alluvial fans from Digital Elevation Models with a GIS algorithm for the geomorphological mapping of the Earth and Mars. Geomorphology 273, 134–149. URL: `https://`

www.sciencedirect.com/science/article/pii/S0169555X16306997, doi:10.1016/j.geomorph.2016.08.010.

Obermeyer, K.J., Yu, C., Stefanie, T., Ramiro, C., 2008. VisiLibity: A C++ Library for Visibility Computations in Planar Polygonal Environments. URL: http://www.VisiLibity.org.

Parker, G., Paola, C., Whipple, K.X., Mohrig, D., 1998. Alluvial Fans Formed by Channelized Fluvial and Sheet Flow. I: Theory. Journal of Hydraulic Engineering 124, 985–995. URL: https://ascelibrary.org/doi/abs/10.1061/%28ASCE%290733-9429%281998%29124%3A10%28985%29, doi:10.1061/(ASCE)0733-9429(1998)124:10(985).

Pauli, N.S., Gioia, G., 2007. The topography of steady sandpiles on arbitrary domains. Proceedings of the Royal Society A: Mathematical, Physical and Engineering Sciences 463, 1247–1258. URL: https://royalsocietypublishing.org/doi/10.1098/rspa.2007.1812, doi:10.1098/rspa.2007.1812.

Reynolds, T., 2024. Grain size from source to sink – modern and ancient fining rates. Earth-Science Reviews 250, 104699. URL: https://www.sciencedirect.com/science/article/pii/S0012825224000266, doi:10.1016/j.earscirev.2024.104699.

Rice, S.P., Church, M., 2001. Longitudinal profiles in simple alluvial systems. Water Resources Research 37, 417–426. URL: https://www.scopus.com/inward/record.uri?eid=2-s2.0-0035141779&doi=10.1029%2f2000WR900266&partnerID=40&md5=eb692b77c4767f3e31441fafd4f3fff0, doi:10.1029/2000WR900266.

Rickenmann, D., 2005. Runout prediction methods, in: Debris-flow Hazards and Related Phenomena. Springer Berlin Heidelberg, Berlin, Heidelberg, pp. 305–324. URL: https://doi.org/10.1007/3-540-27129-5_13, doi:10.1007/3-540-27129-5_13.

Saito, K., Oguchi, T., 2005. Slope of alluvial fans in humid regions of Japan, Taiwan and the Philippines. Geomorphology 70, 147–162. URL: https://

www.sciencedirect.com/science/article/pii/S0169555X05001406, doi:10.1016/j.geomorph.2005.04.006.

Seybold, H., Berghuijs, W.R., Prancevic, J.P., Kirchner, J.W., 2021. Global dominance of tectonics over climate in shaping river longitudinal profiles. Nature Geoscience 14, 503–507. URL: https://doi.org/10.1038/s41561-021-00720-5, doi:10.1038/s41561-021-00720-5.

Shiu, W.J., Lee, C.F., Chiu, C.C., Weng, M.C., Yang, C.M., Chao, W.A., Liu, C.Y., Lin, C.H., Huang, W.K., GeoPORT Working Group, 2023. Analyzing landslide-induced debris flow and flow-bridge interaction by using a hybrid model of depth-averaged model and discrete element method. Landslides 20, 331–349. URL: https://doi.org/10.1007/s10346-022-01963-y, doi:10.1007/s10346-022-01963-y.

Staley, D.M., Wasklewicz, T.A., Blaszczynski, J.S., 2006. Surficial patterns of debris flow deposition on alluvial fans in Death Valley, CA using airborne laser swath mapping data. Geomorphology 74, 152–163. URL: https://www.sciencedirect.com/science/article/pii/S0169555X05002655, doi:10.1016/j.geomorph.2005.07.014.

Stanistreet, I., McCarthy, T., 1993. The Okavango Fan and the classification of subaerial fan systems. Sedimentary Geology 85, 115–133. URL: https://linkinghub.elsevier.com/retrieve/pii/003707389390078J, doi:10.1016/0037-0738(93)90078-J.

Troeh, F.R., 1965. Landform equations fitted to contour maps. American Journal of Science 263, 616–627. doi:10.2475/ajs.263.7.616.

Van Der Walt, S., Schönberger, J.L., Nunez-Iglesias, J., Boulogne, F., Warner, J.D., Yager, N., Gouillart, E., Yu, T., 2014. scikit-image: image processing in Python. PeerJ 2, e453. URL: https://peerj.com/articles/453, doi:10.7717/peerj.453.

Vincent, L.T., Eaton, B.C., Leenman, A.S., Jakob, M., 2022. Secondary Geomorphic Processes and Their Influence on Alluvial Fan Morphology, Channel Behavior and Flood Hazards. Journal of Geophysical Research: Earth Surface 127, e2021JF006371. URL: `https://agupubs.onlinelibrary.wiley.com/doi/abs/10.1029/2021JF006371`, doi:`10.1029/2021JF006371`.

Williams, R.M.E., Zimbelman, J.R., Johnston, A.K., 2006. Aspects of alluvial fan shape indicative of formation process: A case study in southwestern California with application to Mojave Crater fans on Mars. Geophysical Research Letters 33. URL: `https://agupubs.onlinelibrary.wiley.com/doi/abs/10.1029/2005GL025618`, doi:`10.1029/2005GL025618`.

Wu, Y.H., Liu, K.F., Chen, Y.C., 2013. Comparison between FLO-2D and Debris-2D on the application of assessment of granular debris flow hazards with case study. Journal of Mountain Science 10, 293–304. URL: `https://doi.org/10.1007/s11629-013-2511-1`, doi:`10.1007/s11629-013-2511-1`.

Yanagisaki, G., Aono, M., Takenaka, H., Tamamura, M., Nakatani, K., Iwanami, E., Horiuchi, S., Satofuka, Y., Mizuyama, T., 2016. Debris Flow Simulation by Applying the Hyper KANAKO System for Water and Sediment Runoff from Overtopping Erosion of a Landslide Dam. International Journal of Erosion Control Engineering 9, 43–57. URL: `https://dx.doi.org/10.13101/ijece.9.43`, doi:`10.13101/ijece.9.43`.

List of Figures

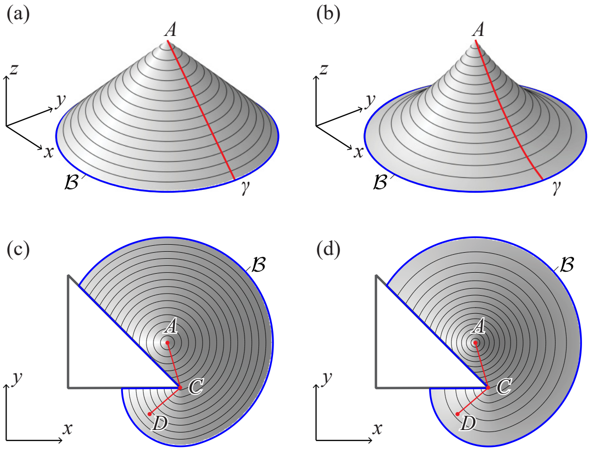

Figure 1: Generatrix determining the shape of the cone with and without obstacle. (a) Constant-slope sand pile generated by the constant slope generatrix. (b) Unconfined fan generated by a curved vertical profile. (c) The plan view of constant-slope sand pile affected by the obstacle. (d) Plan view of confined fan generated by a curved vertical profile; black line: elevation contour; gray line: vertical wall; red line: shortest path line; blue line: fan boundary.

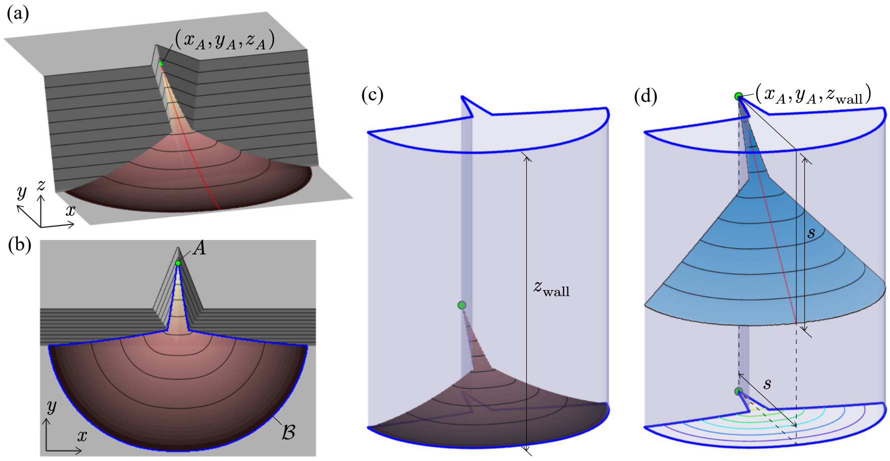

Figure 2: Generation of the shortest path map (SPM). (a) A hypothetical fan showing an elevation-distance relationship (red line) with its apex point (green). (b) The fan boundary, $\mathcal{B}$, displayed in plan view (blue outline). (c) The wall elevation, z_{wall}, imposed beyond $\mathcal{B}$, visualized as the translucent blue wall. (d) The 45° artificial fan surface (blue) yielding the SPM $s(x, y)$ as the elevation drop from z_{wall}.

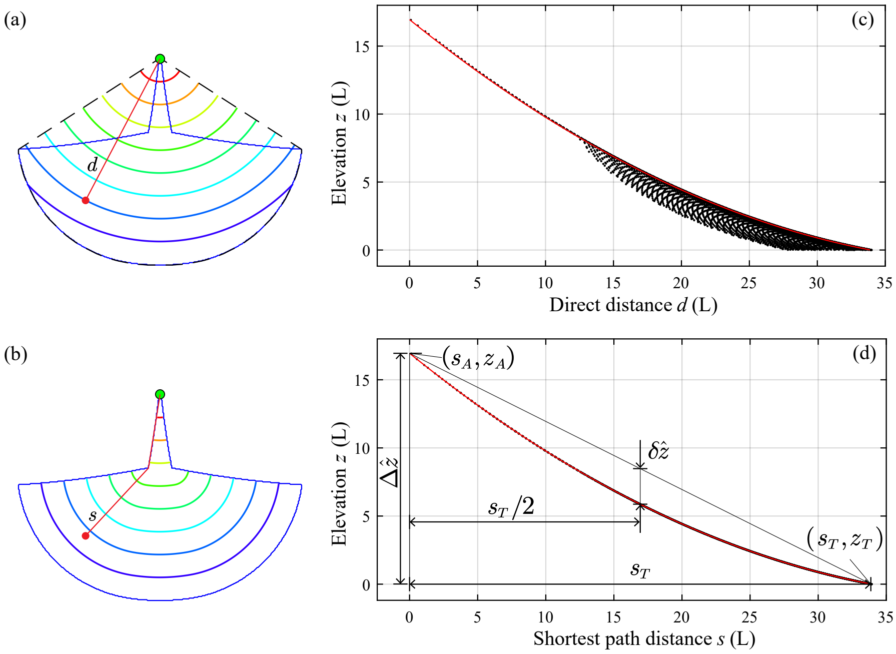

Figure 3: Comparison between direct and shortest path distances and validation of the inverse model. (a) Contours of direct distance from the apex. (b) Contours of shortest path distance from the apex. (c) Scatter plot of direct distance versus elevation. (d) Scatter plot of shortest path distance versus elevation. In panels (c) and (d), the red curve represents the input elevation-distance profile used to generate the hypothetical fan shown in Fig. 2a,b. Panel (d) also defines the different variables used in the morphometric analysis (section 5).

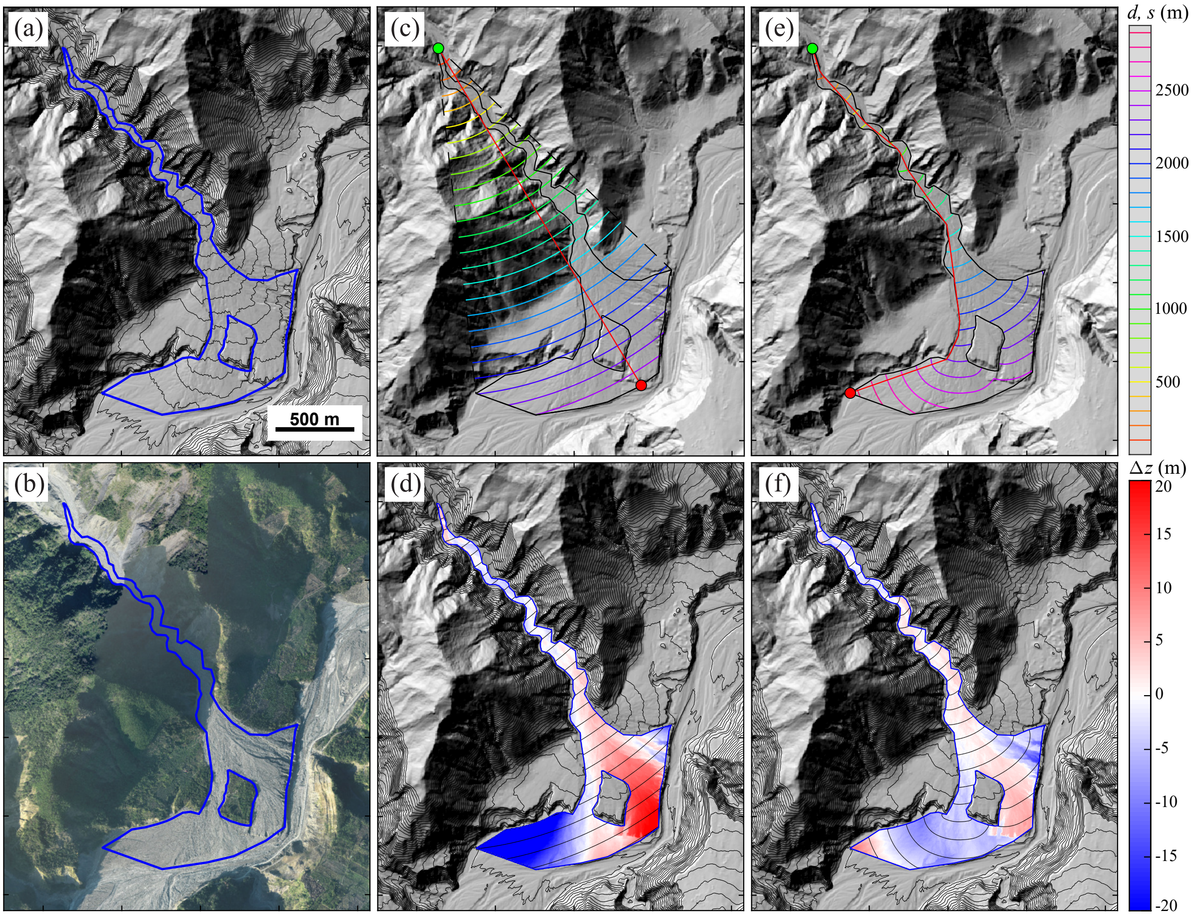

Figure 4: Application of the inverse method to the Putunpunas fan, Laonong River, Taiwan (2014). (a) Hillshade map with 10-meter interval elevation contours. (b) Aerial photography; in both (a) and (b), the blue outline indicates the manually defined fan boundary. (c) Direct distance, d, with 100-meter contours in the convex hull (dash line) of the defined boundary (black outline); red line: direct path line from apex to the farthest point (red dot). (d) Elevation difference Δz between the direct distance reconstructed topography and the surveyed topography within the defined boundary (blue outline), with 10-meter interval contours of direct distance reconstructed topography. (e) Shortest path distance, s, with 100-meter contours in the defined boundary; red line: shortest path from apex to farthest point. (f) Elevation difference Δz between the shortest path distance reconstructed topography and the surveyed topography within the defined boundary (blue outline), with 10-meter interval contours of shortest path distance reconstructed topography.

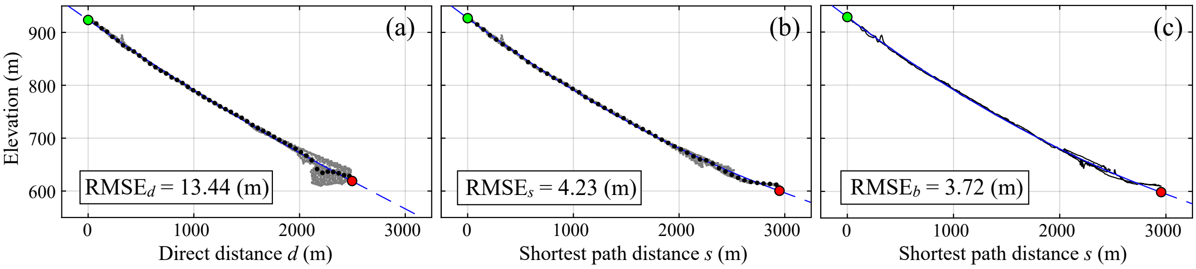

Figure 5: Elevation-distance relationships for the Putunpunas fan. The distance from the apex is calculated using three methods: (a) direct distance, (b) shortest path distance to all data points, and (c) shortest path distance to the boundary points. In panels (a) and (b), gray dots represent all elevation-distance data pairs, and black dots show the median elevation within 50 equal-sized distance bins. A quadratic polynomial (solid blue line), with a tangential extension (dashed blue line), is fitted to the binned data (black dots). The Root Mean Square Error (RMSE) shown on each panel quantifies the deviation between this fitted curve and the original elevation-distance data. The fan apex and the farthest point are marked by red and green circles, respectively. In panel (c), the solid black line connects the boundary data points.

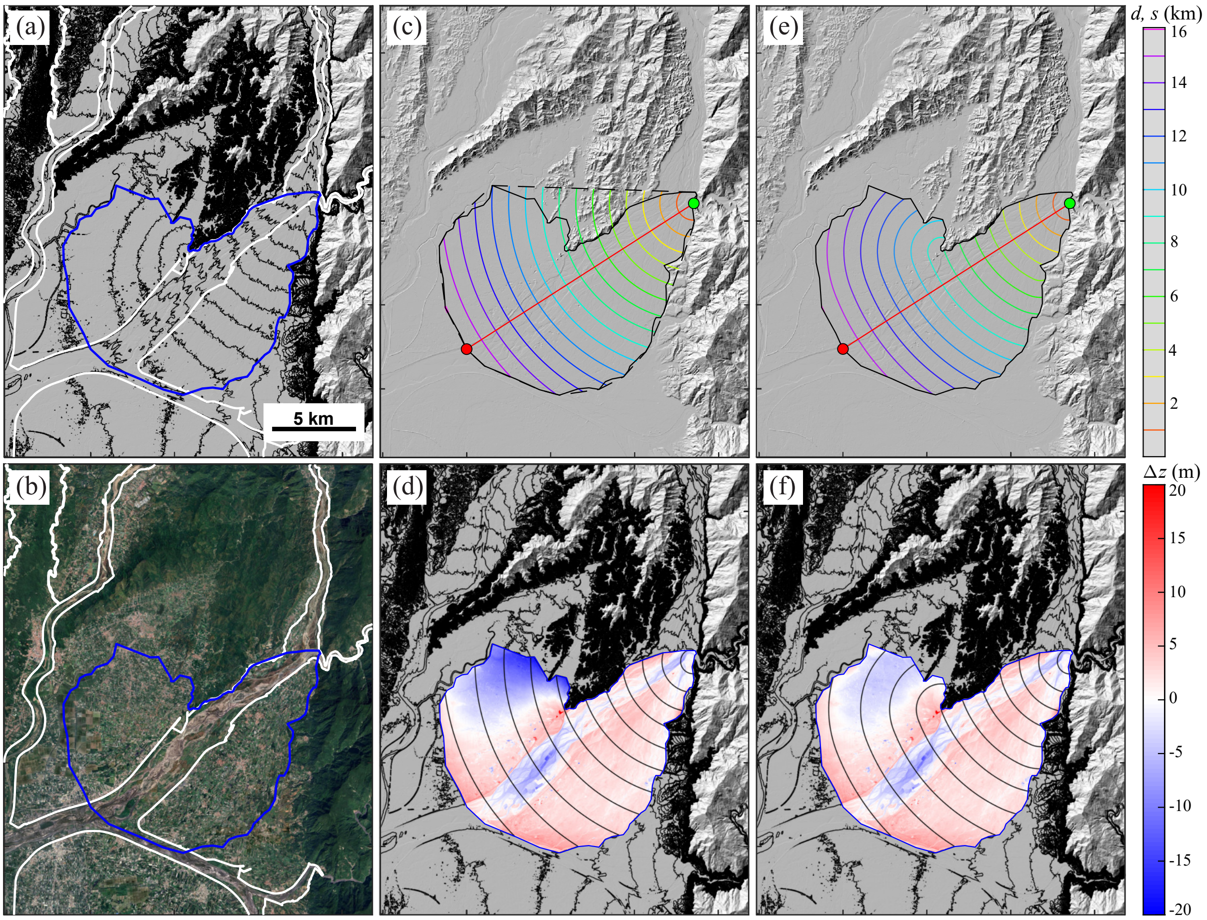

Figure 6: Application of the inverse method to the large Laonong River fan, Taiwan. (a) Hillshade map with 10-meter interval contours. (b) Aerial photography; in both (a) and (b), the blue outline indicates the manually defined fan boundary, and the white outline indicates the active river channel, which was excluded from the analysis. (c) Direct distance, d, with 1000-meter contours in the convex hull of the defined boundary (black outline); red line: direct path line from apex to the farthest point (red dot); dashed line: convex hull of the manually defined fan boundary. (d) Elevation difference Δz between the direct distance reconstructed topography and the surveyed topography within the defined boundary (blue outline), with 10-meter interval contours of direct distance reconstructed topography. (e) Shortest path distance, s, with 1000-meter contours in the defined boundary; red line: shortest path from apex to farthest point. (f) Elevation difference Δz between the shortest path distance reconstructed topography and the surveyed topography within the defined boundary (blue outline), with 10-meter interval contours of shortest path distance reconstructed topography.

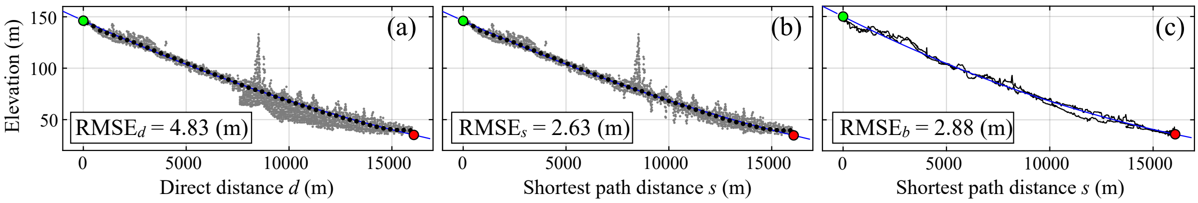

Figure 7: Elevation-distance relationships for the Laonong River fan. Unlike the previous analysis, data points from the active river channel have been excluded. All other methods and symbols are as described in the caption for Fig. 5.

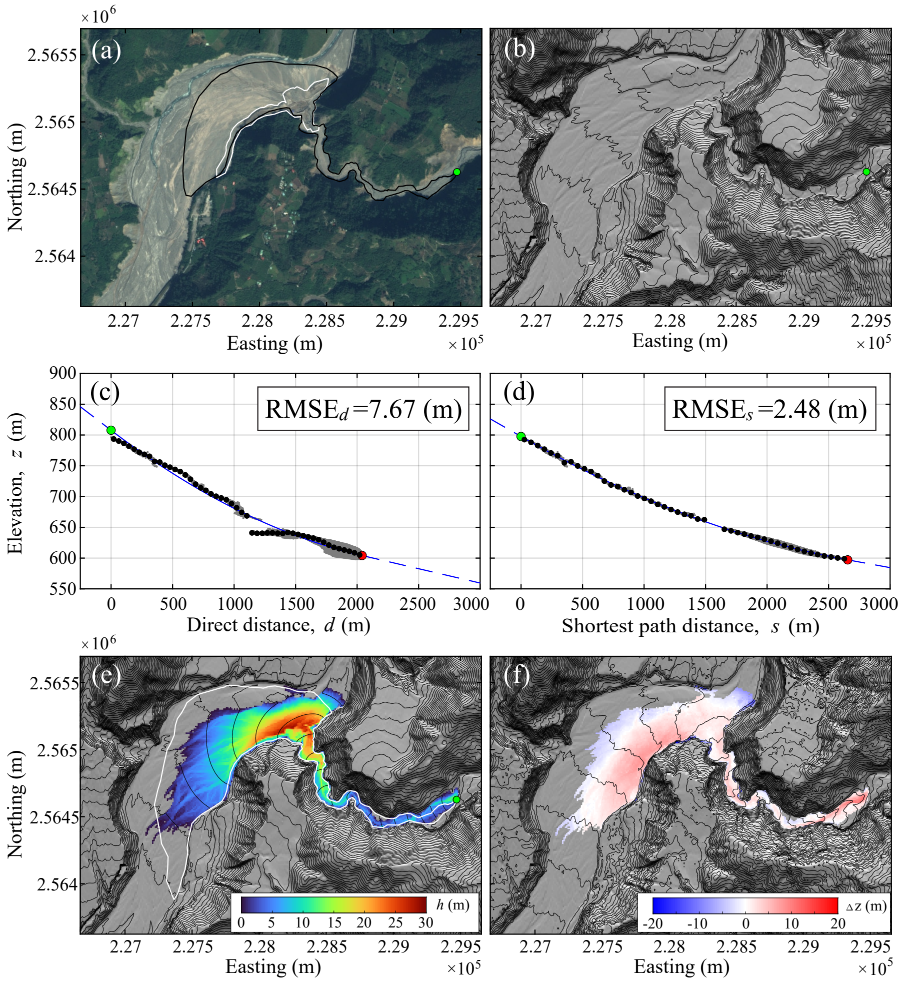

Figure 8: Fan reconstruction of the 2021/08/07 Yu-Shui fan event. (a) Post-Event Satellite Image (2021/11/07) showing the surface conditions after the event. The black outline delineates the boundary used for the inverse analysis, while the white outline indicates an area excluded due to artificial disturbance. The green circle marks the fan apex. (b) Initial topography z_{init} derived from the minimum DEM values (2016/06/24 and 2022/01/26). The surface is shown with 10-meter contours. The green circle indicates the same fan apex as in (a). (c) Elevation vs. direct distance. (d) Elevation vs. shortest path distance. In panels (c) and (d), data presentation matches Fig. 5a,b; gray data pairs: data outside the white boundary. (e) Contours: reconstructed fan surface showing the forward model's reconstruction based on the quadratic function from panel (d) (contours at 10-meter interval). Color-coded map: deposit thickness h defined as the elevation difference between the reconstructed surface and the initial topography. The white outline marks the fan boundary delineated from immediate post-event contour map and imagery. (f) Reconstruction error defined as the elevation difference Δz between the reconstructed surface and the immediate post-event topography. The coordinate system used is TWD97 / TM2 zone 121 (EPGS:3826).

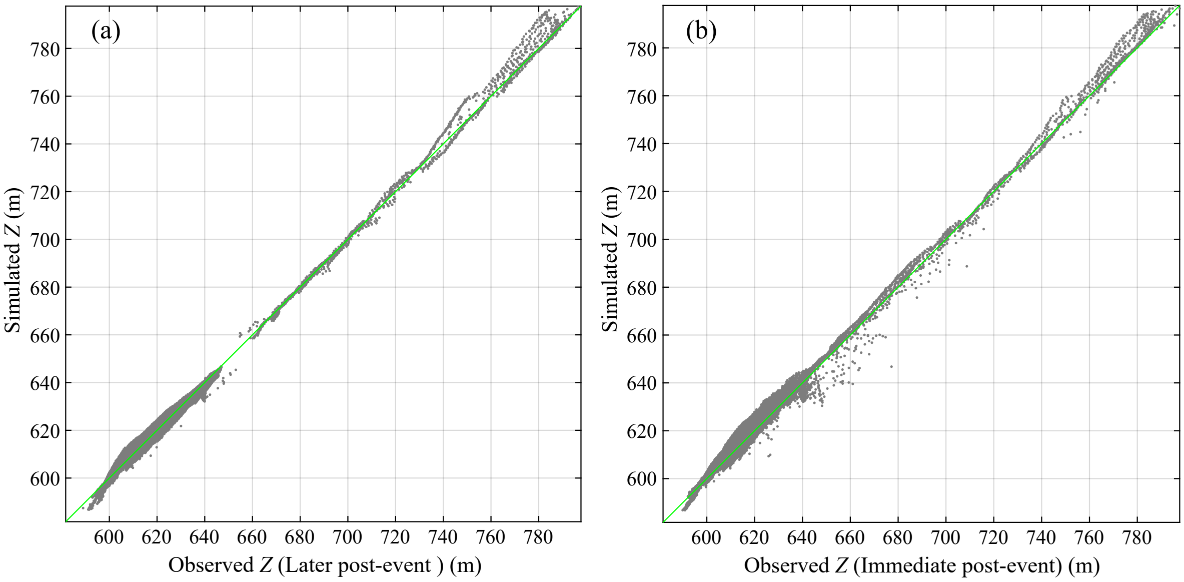

Figure 9: Performance of the fan reconstruction model shown by comparing simulated elevations against two observed datasets. (a) Scatter plot of simulated vs. observed elevations for the later post-event surface (data from 2021/11/07) used for calibration. (b) Scatter plot of simulated vs. observed elevations for the immediate post-event surface (data from 2021/08/12) used for validation. The green line in both panels represents the line of perfect agreement (1:1).

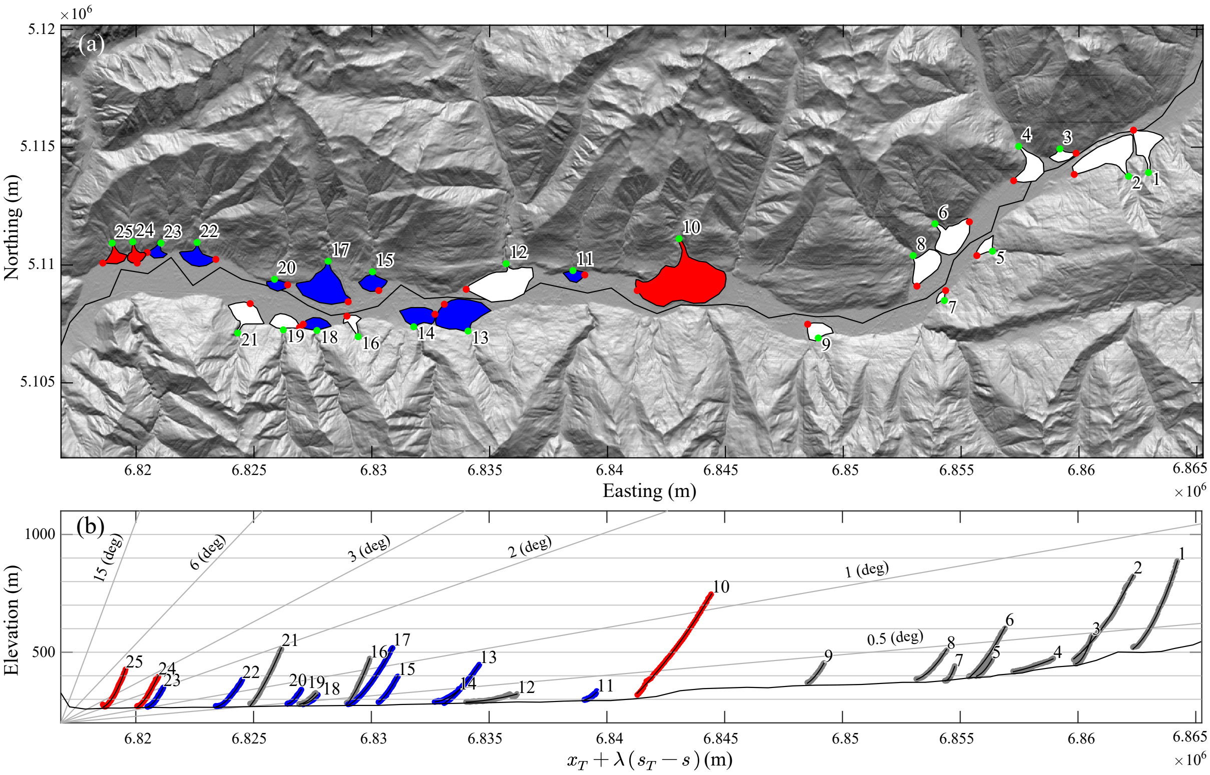

Figure 10: Morphometric analysis of alluvial fans in central Valtellina, Italy. (a) Boundaries of 25 fans, numbered from upstream to downstream. Green dots indicate fan apexes; colored polygons outline the fan planforms; the black line represents the river thalweg. Fan boundaries were delineated following Norini et al. (2016). (b) Elevation profiles of the fans, where the horizontal axis is transformed according to $x = x_T + \lambda(s_T - s)$. Here, x_T represents the x-coordinate of the point farthest from the apex, s_T is the maximum shortest path distance, and s denotes the shortest path distance from the apex. A horizontal scaling factor of $\lambda = 1$ is applied. River and fan profiles are plotted with 10× vertical exaggeration. Colored dots indicate the median elevation within 50 equal-sized bins; the black line represents the riverbed thalweg profile. The coordinate system used is RDN2008 / Italy zone (N–E) (EPSG:6875). Red, blue, and white (gray in panel (b)) colors indicate Type I, Type II, and non-classified fans, respectively, as defined in Crosta and Frattini (2004), where Type I fans are generally characterized by debris-flow processes and Type II fans by fluvial flow processes.

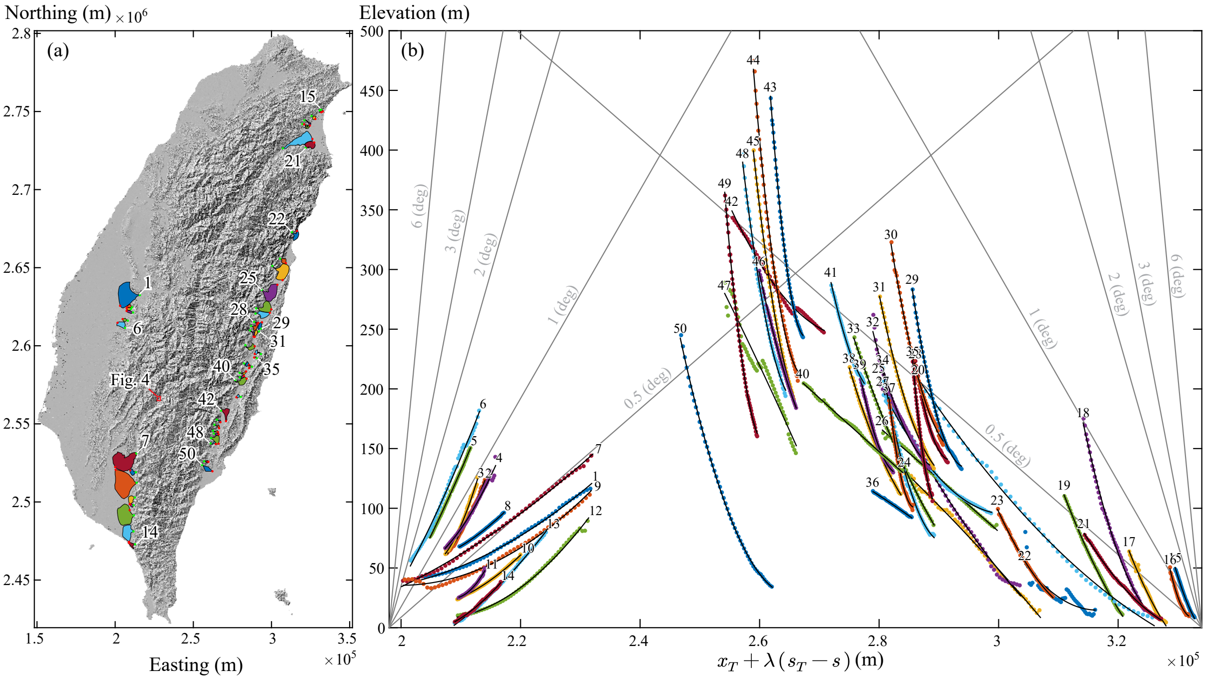

Figure 11: Morphometric analysis of fans in Taiwan. (a) Boundaries of 50 fans, numbered from northwest to southwest and northeast to southeast; green dots: fan apexes; red dots: farthest shortest path distance. The fans are classified based on their terminal conditions: fans 8, 10, 11, and 24-50 are distally confined, while the remainder are distally unconfined. The fan boundaries delineation follows Lin et al. (2009). (b) Elevation profiles of the fans, where the data presentation follows the format of Fig. 10, with a horizontal scaling factor of $\lambda = \pm 2$ applied. Colored dots indicate median elevations within 50 equal-sized bins, with colors corresponding to the fan boundaries in panel (a); black lines: quadratic fits for the median values.

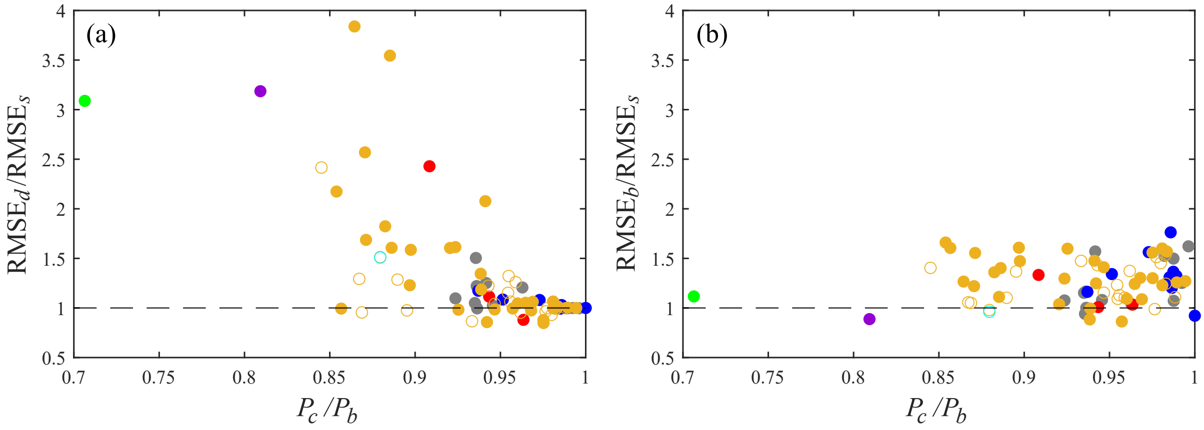

Figure 12: Relationship between the ratio of Root Mean Square Error (RMSE) and the ratio of convex hull perimeter (P_c) to fan boundary perimeter (P_b) for different methods. (a) Relationship between P_c/P_b and the ratio of direct distance RMSE (RMSE$_d$) to shortest path distance RMSE (RMSE$_s$). (b) Relationship between P_c/P_b and the ratio of boundary shortest path distance RMSE (RMSE$_b$) to RMSE$_s$. Both panels show 50 Taiwanese fans from Lin et al. (2009) (●: distally confined, ○: distally unconfined), including the large Laonong river fan (○), 25 Italian fans from Norini et al. (2016) (●: Type I, ●: Type II, ●: non-classified), the Putunpunas fan (●), and the Yu-Shui fan (●).

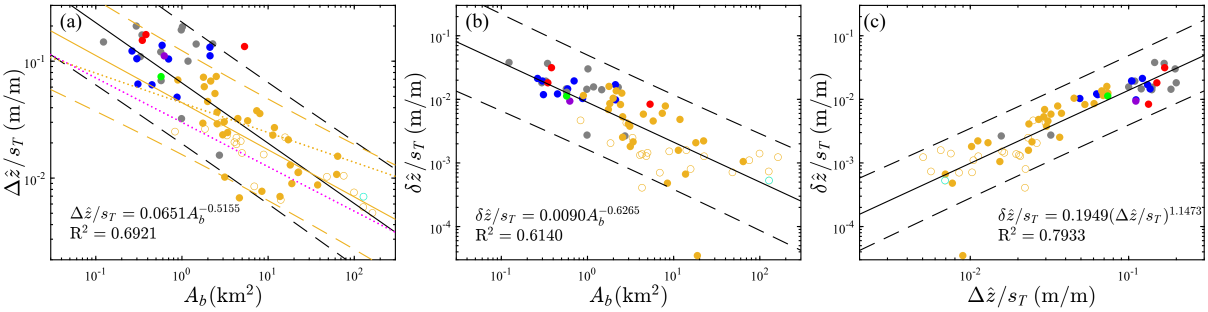

Figure 13: Log-log relationships of fan morphometric properties for 50 Taiwanese fans from Lin et al. (2009) (●: distally confined, ○: distally unconfined), including the Laonong river fan (○), 25 Italian fans from Norini et al. (2016) (●: Type I, ●: Type II, ●: non-classified), the Putunpunas fan (●), and the Yu-Shui fan (●). (a) Regression of fan area A_b versus slope $\Delta\hat{z}/s_T$. The black line shows the overall regression for all 77 data points, with dashed black lines indicating the 95% confidence interval. The yellow line represents the regression for the 50 Taiwanese fans, with yellow and black dashed lines showing the 95% confidence interval. Comparisons are included with regression results from previous studies (yellow dotted line from Lin et al. (2009) and magenta dotted line from Saito and Oguchi (2005)). (b) Relationship between dimensionless drop $\delta\hat{z}/s_T$ and fan area A_b, where the black line represents the overall regression, and dashed lines indicate the 95% confidence interval. (c) Relationship between slope $\Delta\hat{z}/s_T$ and dimensionless drop $\delta\hat{z}/s_T$, with the black line showing the overall regression and dashed lines representing the 95% confidence interval.